Journal of Materials Chemistry C

ROYAL SOCIETY OF CHEMISTRY

PAPER

View Article Online
View Journal | View Issue

Cite this: J. Mater. Chem. C, 2025, 13, 14902

An ultrathin, transparent, flexible, and self-powered photodetector based on two-dimensional materials and a self-assembled polar-monolayer

Meng-Ching Lai,[a] Jia-Yu Lin,[a] Yu-Chieh Chao,[a] Chia-Chun Ho,[a] Fang-Chi Hsu,*[b] Ji-Lin Shen*[c] and Yang-Fang Chen*[a]

Received 8th April 2025,
Accepted 7th June 2025

DOI: 10.1039/d5tc01465d

rsc.li/materials-c

Flexibility, transparency and self-powered operation are three desirable features for the practical application of advanced photodetectors. In this work, an ultrathin, flexible, self-powered, and transparent photodetector made from all two-dimensional (2D) materials with a polar monolayer is proposed and demonstrated. This device consists of a layer of graphene serving as a transparent electrode, a single-layer tungsten disulfide (WS_2) acting as a light-absorbing layer, a self-assembled monolayer (SAM) of P3HT-COOH with polar properties to provide an additional built-in electric field, and an indium-tin-oxide (ITO) coated polyethylene terephthalate (PET) flexible substrate. The average transmittance in the visible light regime is around 67%. Under zero bias voltage, the photodetector exhibits a responsivity of 1.58 mA W^{-1} and a detectivity of 3.29 $\times$ 10^9 Jones. Additionally, this flexible photodetector demonstrates good retention, retaining its original responsivity magnitude after 150 bending cycles without too much significant change. Based on the aforementioned properties, this ultrathin, transparent, flexible, and self-powered photodetector based on all 2D materials with a polar monolayer offers an attractive option for developing advanced optoelectronic technologies.

Introduction

Photodetectors are commonly encountered in daily life and find applications in electro-optical displays, biomedical sensing, telecommunications, *etc.*[1–4] Silicon (CMOS-based) photodetectors have been widely employed commercially due to their high performance, cost-effectiveness and mature technologies.[2] Typical organic material-based photodetectors have achieved rapid development with EQE $\gg$ 100% and a tunable spectral response range.[5–7] In recent years, there has been a notable increase in the research and the applications of photodetectors composed of two-dimensional (2D) materials. Compared with conventional materials used in photodetectors, 2D materials are competitive because they possess high carrier mobility, broadband absorption and flexibility, allowing applications in flexible and wearable devices.

Graphene, with its superior optical and electrical properties, is commonly utilized in the study of optoelectronic devices, including transistors, photodetectors, *etc.*[8,9] Other types of 2D materials, such as transition metal dichalcogenides, layered semiconductors, and perovskites, are also suitable for diverse roles in optoelectronic devices such as electrodes, photogate layers and light-absorbing layers.[7–11] The combinations of graphene and other 2D materials have been studied and employed in multiple photovoltaic applications.[12–15] In these applications, 2D materials serve as photoactive materials and graphene functions as the transparent electrode. The vertical heterostructure formed by graphene and the 2D material provides a large active area and facilitates the rapid transfer of charge carriers from the 2D material to graphene.[16–19] Tungsten disulfide (WS_2), one of the transition metal dichalcogenides, possesses a direct bandgap in the visible range and exhibits strong light–matter interaction, making it an excellent candidate for the light-absorbing material in photodetectors.[20–23] Photodetectors employing WS_2/graphene heterostructures demonstrated high performance, attributed to the presence of the built-in electric field arising from the difference in Fermi levels between WS_2 and graphene.[24–27]

The working principle of photodetectors relies on the photovoltaic effect, where the migration of charge carriers is driven

[a] Department of Physics, National Taiwan University, Taipei 106, Taiwan. E-mail: 123123123mm@gmail.com, j32880424@gmail.com, a86112727@gmail.com, jack.ho99116@gmail.com, yfchen@phys.ntu.edu.tw
[b] Department of Materials Science and Engineering, National United University, Miaoli 360, Taiwan. E-mail: fangchi@nuu.edu.tw
[c] Department of Physics and Research Center for Crystalline Materials, and Optoelectronic Characterization, Chung Yuan Christian University, ChungLi 32023, Taiwan. E-mail: jlshen@cycu.edu.tw

by the built-in electric field within the photodetectors themselves. Generally, a bias is applied to photodetectors to efficiently extract the charge carriers. When no power is supplied (or zero bias), photodetectors operate in self-powered modes. This self-powered property enhances the portability of the whole system and thus has great application potential to be applied in wireless sensor networks and wearable electronics. There are different ways to produce a built-in electric field. For instance, it can be generated by the formation of a Schottky barrier, a p–n junction, or a polar monolayer.[28–31] The Schottky barrier typically forms between the electrode and the substrate or between a 2D heterojunction of metallic and semiconducting materials. It was found[31–39] that the self-assembled monolayer (SAM) of poly[3-(6-carboxyhexyl)thiophene-2,5-diyl] (P3HT-COOH) on the surface of indium-tin-oxide (ITO) resulted in an oriented dipole layer. This SAM of P3HT-COOH has been realized in both perovskite photodetectors and perovskite solar cells with high performances due to the presence of the dipole layer.[29–31]

In this work, we fabricated a photodetector comprising graphene, single-layer tungsten disulfide (WS_2), SAM of P3HT-COOH, and a patterned ITO-coated polyethylene terephthalate (PET) flexible substrate. The high transmittance of the photodetector was found, showing the transparent nature of the whole device. The built-in electric fields generated by the WS_2/graphene heterostructure and the SAM were oriented in the same direction, facilitating the movement of photoinduced charge carriers. The impact of the property of the polar SAM is to sweep hole charges to the ITO electrode due to its dipole field induced during the self-assembly such that the photocurrent and photoresponse time can largely be improved. The flexibility of the photodetector was also evaluated by measuring its performance under curvature and various bending cycles. Utilizing the properties of 2D materials, the polar nature of the self-assembled monolayer of P3HT-COOH molecules, and the bendable substrate, we have successfully demonstrated a highly transparent, flexible, self-powered photodetector based on all 2D materials with good performance. Photodetectors with ultrathin, transparent, self-powered, and flexible features offer an attractive option for future wearable and other advanced optoelectronic technologies.

Results and discussion

Properties of materials used

To obtain the qualities of the materials comprising the device, the Raman spectra of graphene, WS_2 and WS_2/graphene were analyzed. Samples of graphene were prepared by the wet-transfer technique onto a Si/SiO_2 substrate. The Raman spectra were all measured under 532 nm laser excitation. Fig. 1a depicts the Raman spectrum of graphene, revealing the respective peaks of the D-band, G-band and 2D-band at 1342 cm^{-1}, 1587 cm^{-1} and 2683 cm^{-1}. The intensity ratio of 2D-band to

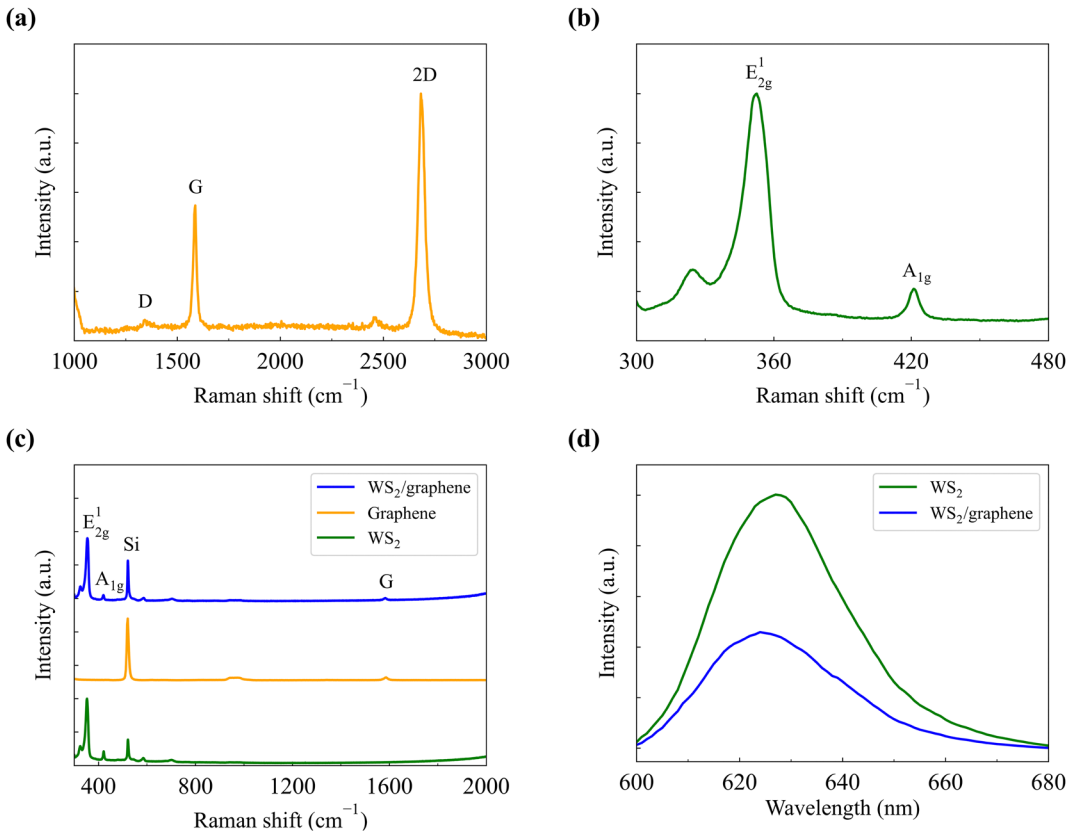

Fig. 1 Raman spectra of (a) graphene, (b) WS_2, and (c) graphene, WS_2, and WS_2/graphene. (d) Photoluminescence spectra of WS_2 and WS_2/graphene.

G-band is approximately 1.8, and that of D-band to G-band is approximately 0.1, which is negligible. This indicates that the synthesized graphene is of high-quality and monolayer.[32,33] Fig. 1b presents the Raman spectrum of WS_2, displaying peaks of the in-plane E^1_{2g} vibration mode and the out-of-plane A_{1g} vibration mode at 353 cm^{-1} and 421 cm^{-1}, respectively, which are consistent with the previous reports.[21,23] For WS_2/graphene, it exhibits both spectrum features of graphene and WS_2 in addition to the peak from the Si/SiO_2 substrate at 520 cm^{-1} (Fig. 1c). The result confirms a successful transfer of a single-layer graphene onto the monolayer WS_2. The peak position of the E^1_{2g} mode in WS_2/graphene is the same as that of the bare WS_2, revealing that the in-plane vibration mode remains unaffected by the interaction induced by graphene.[34] However, the peak position of the A_{1g} mode and the G-band peak exhibited a small red-shift of 1.5 cm^{-1} and 2.3 cm^{-1}, respectively. The red-shift can be explained by the charge transfer between WS_2 and graphene.[34–36]

Photoluminescence (PL) spectra were recorded to further study the optical and electrical properties of the materials in the photodetectors. Fig. 1d displays the PL spectra of WS_2 and WS_2/graphene under 374 nm light excitation. The PL peak of WS_2 was located at around 627 nm, corresponding to a band-gap of about 1.98 eV, whereas that of WS_2/graphene exhibited a subtle blue-shift to 624 nm. Additionally, the peak intensity of the bilayer sample was weaker than that of bare WS_2. The blue-shift and PL quenching can be attributed to the charge transfer between WS_2 and graphene due to the built-in electric field originating from the difference in work functions, thereby suppressing charge recombination.[37–40] It is noted that, according to the previous studies, the work functions of graphene and WS_2 are 4.7 eV and 4.86 eV, respectively.[20,41]

Properties of graphene/WS_2/SAM photodetectors

Fig. 2a presents the schematic illustration of the photodetector comprising a patterned ITO substrate, a hole transport layer of SAM of P3HT-COOH, a 2D WS_2 film, and a graphene layer. The liquid-phase deposition of P3HT-COOH molecules allows the carboxylic groups to rotate freely and orient themselves toward the ITO surface. This increases the anchoring density of the carboxylic groups on the electrode surface, thereby forming a highly oriented electric dipole layer and showcasing an electric field directed toward the ITO surface, making it an efficient hole-transport layer as shown in our previous report.[38] The WS_2 monolayer, acting as a light-absorbing layer, features a Fermi level of −4.86 eV. After contact, since graphene has a work function smaller than WS_2, holes then injected into graphene from WS_2 to align the Fermi level and therefore caused a

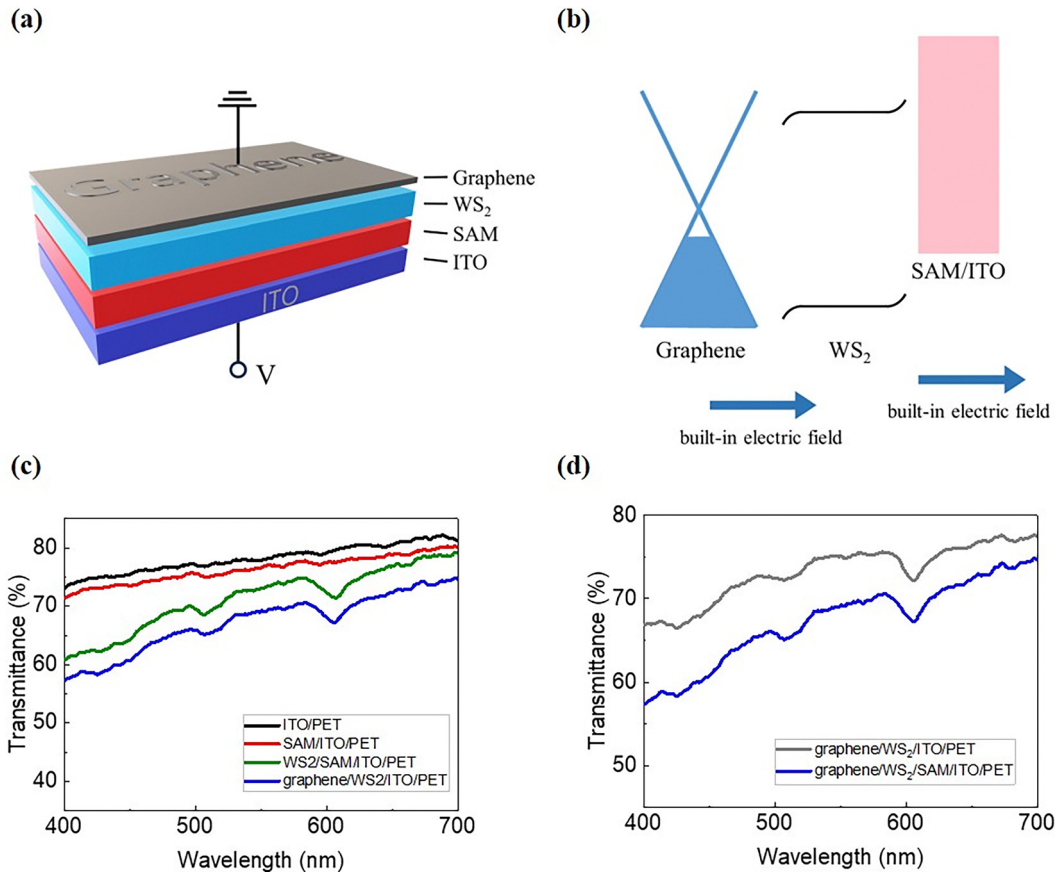

Fig. 2 (a) Schematic illustration of the fabricated photodetector with a self-assembled monolayer (graphene/WS_2/SAM/ITO). (b) The energy level diagram for the device with the SAPM illustrating the direction of the built-in electric fields after contact. (c) Optical transmission spectra of each layer in the photodetector. (d) Comparison of optical transmission for photodetectors with and without incorporating SAM.

down-shift of the graphene Fermi level and induced a built-in electric field pointing from graphene toward WS_2. For the device with the polar SAM, the monolayer dipole of the P3HT-COOH molecules produced an electric field pointing toward the ITO substrate, which is in the same direction as the built-in electric field arising from the WS_2/graphene heterojunction.[29–31] The energy band diagram, illustrating the direction of the built-in electric fields after contact, is shown in Fig. 2b.

The transparency of the device can be determined by optical transmission measurements. Fig. 2c illustrates the optical transmission spectra of ITO, SAM/ITO, WS_2/SAM/ITO and graphene/WS_2/SAM/ITO within the wavelength range of 400 to 700 nm. The average transmittance of the photodetector with the polar SAM was around 67% in the visible light regime (400–700 nm) while that of the one without the SAM showed a higher average transmittance of 73% (Fig. 2d).

Device performance

When determining the performance of photodetectors, various figure-of-merits parameters, including responsivity (R), specific detectivity (D^*) and photocurrent response time (time interval between a change from 10% to 90% of maximum photocurrent), are utilized as benchmarks.

To evaluate the photoresponse performances of the devices, they were illuminated under a 325 nm helium–cadmium laser with a power density of 16.14 mW cm^{-2} at 0 V. The reason we chose a 325 nm laser as the illumination light source is that it is within the absorption wavelength regime of WS_2 nanosheets from 300 nm to 900 nm.[42] As the photodetection mechanism is illustrated schematically in Fig. 3a, the electron–hole pairs were generated in WS_2 upon photoexcitation, and the build-in electric field produced by graphene/WS_2 enabled the charge carriers to travel to the respective electrode in the absence of the applied voltage. For devices with SAM layers, the electric field generated by the polar monolayer can rapidly sweep hole charges to ITO electrodes for collection. Fig. 3b shows the 4-cycle temporal responses of devices with and without the polar SAM under the switching on and off the light source at every 5 s. The device with the polar SAM possessed a higher photocurrent. The rise and fall times determining the response times of the photodetectors with and without the polar SAM were less than 200 ms. We point out here that, due to the instrumental limit, we do not have sufficient resolution to resolve the actual response times for both types of devices. However, it is expected that the response time is faster for the device with the polar SAM because of the more effective electron–hole separation

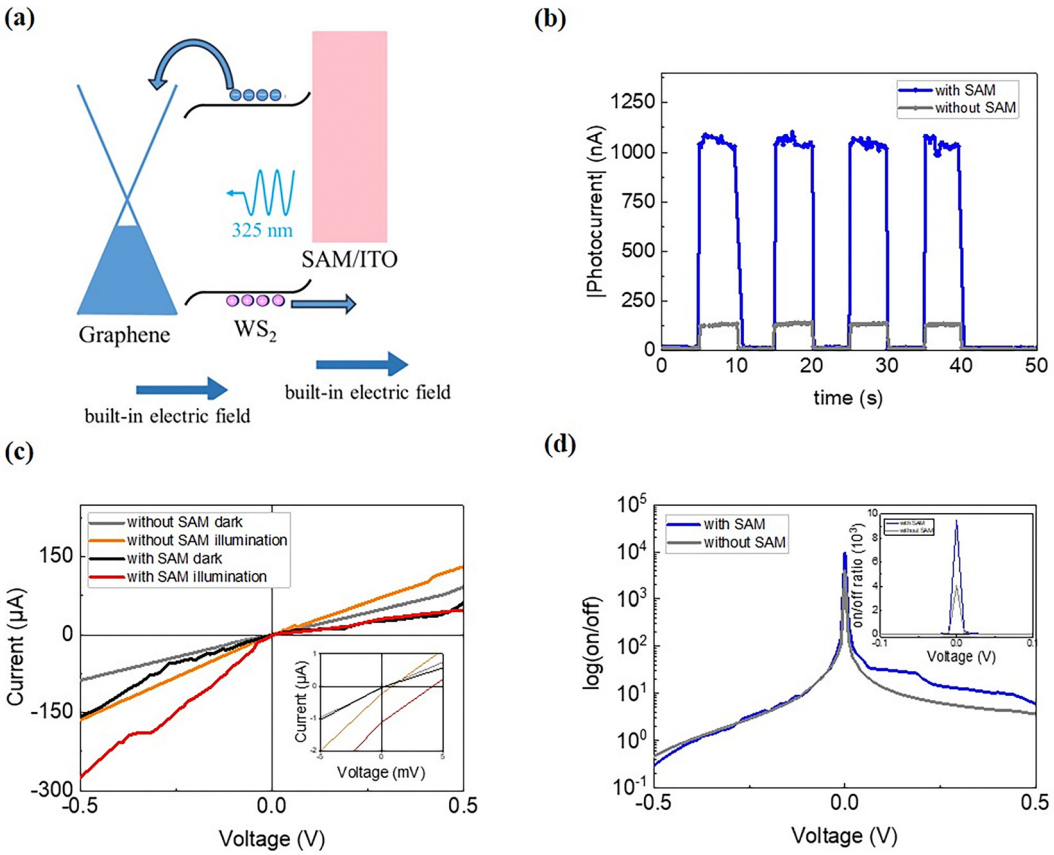

Fig. 3 (a) Schematic band diagram of the device with the SAM under excitation from a 325 nm laser at zero bias. (b) Temporal responses of photodetectors under excitation from a 325 nm laser at 0 V. (c) Current–voltage characteristic curves of photodetectors in the dark and under 325 nm light illumination. The inset shows a zoomed-in chart around 0 V. (d) On/off ratio as a function of bias voltages from −0.5 V to +0.5 V for the best device plotted in a logarithmic scale on the y-axis. The inset is the zoom-in chart around 0 V plotted with the y-axis in a linear scale.

assisted by the polar built-in electric field. The responsivity R can be obtained from the formula[43] $R = \frac{I_{ph} - I_d}{P_{in}}$, where I_{ph}, I_d, and P_{in} represent the photocurrent, the dark current, and the input power, respectively. Detectivity (D^*) is determined by the responsivity and noise current. Generally, the noise current includes both shot noise and thermal noise. The shot noise can be found from $(2eI_dB)^{1/2}$,[44–47] where e is the elementary charge, I_d stands for the dark current, and B is the bandwidth and the thermal noise can be obtained from $(4k_BTB/R)^{1/2}$,[44–48] where k_B, T, and R are the Boltzmann's constant, temperature, and the resistance of the device at a specific voltage, respectively. The noises for photodetectors with and without the SAM biased at 0 V were calculated to be 1.6 and 1.8 pA $Hz^{-1/2}$, respectively, which were much lower than the measured dark current of ~20 nA. The D^* value can be calculated from the equation[49] $D^* = \frac{R}{\sqrt{2 \times e \times J_d}}$, where R is the responsivity, e is the elemental charge, and J_d is the dark current density. The R and D^* values for the device with the polar SAM were calculated to be 1.58 mA W^{-1} and 3.29 × 10^9 Jones, respectively, demonstrating superior performance to the one without the polar SAM having a R value of 0.17 mA W^{-1} and a D^* value of 2.94 × 10^8 Jones. Both the R and D^* values of the photodetector without the polar SAM are comparable to the previously reported WS_2-based photodetectors with similar device structures.[50–53]

The current–voltage (I–V) characteristic curves of photodetectors in the dark and under 325 nm light illumination are shown in Fig. 3c. The inset is the zoom-in chart around 0 V. In this measurement, graphene was grounded and the bias was applied to the ITO electrode. At 0 V, it can be seen that the dark currents are of a few tens nA for both photodetectors, while under irradiation, there are noticeable photocurrents, demonstrating the self-powered functionality. Under forward bias, the external field is in the opposite direction to the built-in electric field and the device with the polar SAM has a smaller dark current than the one without the SAM. When a reverse bias was applied, the device with the polar SAM exhibited a relatively larger dark current due to the electric field produced by the polar SAM. Under illumination, the reverse bias can efficiently separate the photogenerated carriers in WS_2 and the build-in electric field produced by the polar SAM layer can rapidly sweep hole charges to be collected at the ITO electrode, resulting in a larger photocurrent response. Fig. 3d exhibits the photocurrent-to-dark current ratio *vs.* voltage characteristic curves for another set of devices, showing the subtle increase in the on/off ratio for devices with the SAM in the reverse bias, but a significant improvement at 0 V. At 0 V, the on/off ratio of the photodetector with the polar SAM is approximately 1.4 times greater than that of the one without the polar SAM (the inset of Fig. 3d). This result is also consistent with the findings shown in Fig. 3b.

The proposed photodetector should be able to respond to light of sufficiently high intensity and the corresponding state-of-the-art parameters can be obtained. According to the published reports, the response time is faster at higher light intensity due to defect trapping, while the responsivity and detectivity decrease with increasing light intensity arising from less effective electron–hole separation.[54] In our study, we focus more on the impact of the introduced polar SAM on the photodetectors operating in the self-powered mode. Based on the above results, the presence of the polar SAM significantly enhances the overall performance of the device. The underlying physics can be understood as follows. As the built-in electric field from the monolayer dipole in the SAM aligns with the one formed by the WS_2/graphene heterostructure, the devices with the polar SAM exhibit a stronger internal electric field in contrast to those without the polar SAM. The greater the combined built-in electric field in the device, the lower the recombination of photoexcited electrons and holes. This results in more charge carriers collected at the electrodes in the device with the polar SAM, leading to the improved photocurrent, photoresponsivity, and detectivity.

Flexibility tests and applications of optical communication

In this study, the materials comprising the devices, including the graphene electrode, the WS_2 active layer, and the hole transport layer of the polar SAM, are all monolayer. Therefore, by employing mechanically bendable ITO/PET substrates, it is promising to develop flexible photodetectors based on all 2D materials. The flexibility was characterized by measuring the responsivity under a certain curvature and different bending cycles. Fig. 4 illustrates the normalized temporal responses of the photodetector at flat and under bending at a bending radius of 1.6 cm with the associated optical image shown in the inset, demonstrating the bending capability of the photodetector. The device was in a laser focus when it was flat. During a bending test with a radius of 1.6 cm, the photodetector maintained about 40% of its original responsivity. This reduced performance may be attributed to the shift in the laser focus point and changes in the incident angle of the light illumination under bending measurements, because we did not re-adjust the laser focus on the device. Fig. 5a displays the

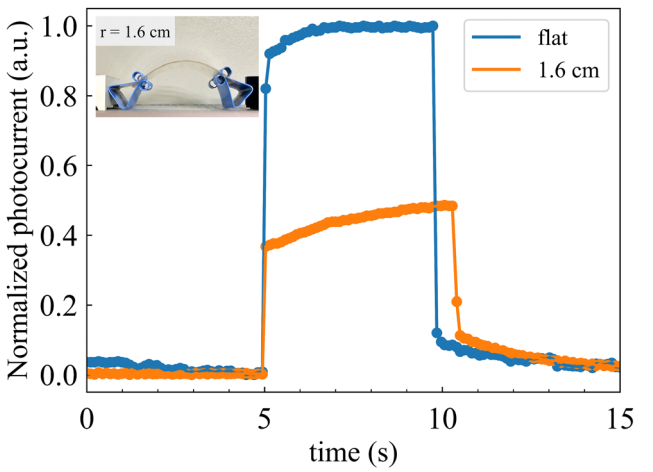

Fig. 4 Temporal responses at 0 V under a radius of curvature of 1.6 cm (inset: the optical image of the photodetector bending at a radius of 1.6 cm).

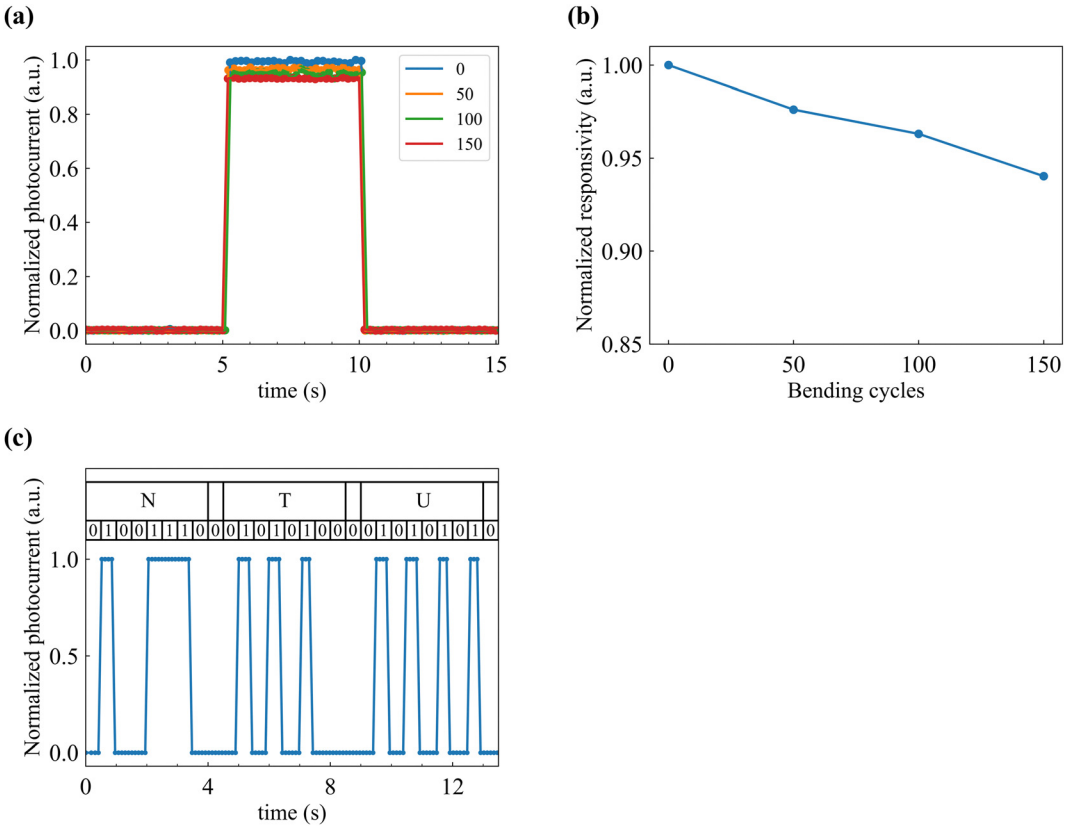

Fig. 5 (a) Temporal responses at 0 V over 150 bending cycles. (b) Normalized responsivities for 150 bending cycles. (c) Temporal response and the corresponding ASCII code conversion of the received data for "NTU".

temporal responses over 150 bending cycles, showing no significant change in the photocurrent when flat, and the photodetector still retained 94% of its original responsivity after 150 bending cycles (Fig. 5b). This indicates that the photodetector has good mechanical stability. Interestingly, a fast response time of around 80 ms of the photodetector facilitates its application in optical communication. Fig. 5c illustrates the temporal response at 0 V and the corresponding ASCII code conversion of the received data. By manipulating the light on and off, a binary signal representing the word "NTU" was generated and detected by the photodetector, where the on state corresponds to 1 and the off state corresponds to 0.

The proposed photodetector features the vertical heterostructure, self-powered, and high transparency (67% on average in the visible regime). Thus, we compare the device performance with those of other opaque, self-powered and/or heterostructured photodetectors reported previously (Table 1). The performance of our proposed photodetector is highly close to those based on organic–inorganic heterojunctions. Compared to those of semitransparent, flexible ones, our proposed device possesses higher detectivity than that reported by Jang *et al.*[52] having a similar structure but carrying a lower transparency (40% on average) than ours. The good performance of our transparent photodetector can be ascribed to the internal dipole field produced by the introduced SAM layer rapidly sweep holes to the electrode for collection.

Table 1 Comparison of the performance parameters with other reported self-powered and/or heterostructured photodetectors

Device structure	Wavelength (nm)	Responsivity (mA W^{-1})	D (Jones)	Ref.
2D perovskite	270	1.2×10^6	$1.4.8 \times 10^{14}$	55
$Ti_3C_3T_x$/GaN	355	284	7.06×10^{13}	56
PANI/ZnO	350	0.56	3.29×10^{10}	57
TiO_2/$PC_{71}BM$/PEDOT:PSS	350	33	1.6×10^{11}	58
ZnO nanofiber	360	1	—	59
Graphene/$MoSe_2$/Si	650	270	7.13×10^{10}	60
WS_2-ND/graphene	550	6400	2.8×10^9	61
Graphene/WSe_2/Au	650	7550	3×10^{12}	62
TSFA-graphene/WS_2	400	140	2.5×10^9	52
ITO/SAM/WS_2/graphene	325	1.58	3.29×10^9	This work

Conclusions

An ultrathin, transparent, flexible, and self-powered photodetector based on graphene, WS_2, and the P3HT-COOH polar monolayer has been successfully fabricated using the wet-transfer technique and self-assembly process. Utilizing an ITO/PET flexible substrate, the photodetector exhibits a high transparency of 67% in the visible light range. The self-powered functionality, resulting from the built-in electric field generated

by the WS_2/graphene heterostructure and the polar SAM, is demonstrated based on the photocurrent response at 0 V. The resulting responsivity and specific detectivity are 1.58 mA W^{-1} and 3.29×10^9 Jones, respectively, which is superior to that of the device without the polar SAM. The impact of the polar SAM is to enhance the separation of photogenerated electron–hole pairs and the photocurrent, which in turn improves the responsivity and detectivity. Furthermore, the photodetector exhibits good mechanical flexibility and retains its original responsivity after 150 bending cycles without too much significant change, demonstrating its flexible capability. Therefore, the ultrathin, flexible, self-powered photodetector based on all 2D materials and the polar SAM shown here should be very useful for the future development of wearable, lightweight, and less power-consuming optoelectronic devices.

Experimental section

Materials

Poly[3-(6-carboxyhexyl)thiophene-2,5-diyl] (P3HT-COOH, MW = 54 KD, Rieke metals Inc.) was purchased commercially. ITO-polyethylene terephthalate (PET) substrates (sheet resistance, 10^{-15} Ω sq^{-1}) were purchased from STAREK Scientific Co., Ltd.

Device fabrication

Patterned ITO/PET substrates underwent 15-min sonication in soap water, deionized water and ethanol in sequence, and were blow-dried with N_2 gas flow. To make the surfaces of the substrates hydrophilic, a 10-min O_2 plasma surface cleaning was performed on the substrates before immersing them in the P3HT-COOH solution for 16 h. Afterward, the substrates were sonicated in *N*,*N*-dimethylformamide (DMF) solution to eliminate residues and form a monolayer on the surface. The WS_2 grown on the SiO_2/Si substrate was first spin-coated with PMMA and then transferred onto the ITO substrate using a typical wet-transfer technique. After removing the PMMA by exposing the substrate to acetone vapor, the graphene grown on copper foil was transferred onto it.

Characterization

Photoluminescence (PL) spectra were measured by using a FluoroMax-4 (HORIBA Ltd) fluorescence spectrometer under 374 nm excitation. Raman spectra were measured by using an iHR550 (HORIBA Ltd) spectrometer under 532 nm excitation. The transmission spectra were measured using a UV-vis spectrophotometer (PerkinElmer LAMBDA 750). The current–voltage (*I*–*V*) characteristics of photodetectors were measured using a Keithley Model 2400 source-power meter at an ultraviolet irradiation (325 nm) intensity of 16.14 mW cm^{-2}. The transient photocurrent responses of the devices were recorded using a Keithley 2400 meter.

Author contributions

The manuscript was written through contributions of all the authors. All the authors have given approval to the final version of the manuscript.

Data availability

Data are available upon request from the authors.

Conflicts of interest

There are no conflicts to declare.

Acknowledgements

This work was financially supported by the National Science and Technology Council in Taiwan (NSTC 112-2112-M-002-030, NSTC 112-2112-M-033-005, NSTC 112-2112-M-239-001, and NSTC 113-2112-M-239-001).

References

1 L. Gu, S. Poddar, Y. Lin, Z. Long, D. Zhang, Q. Zhang, L. Shu, X. Qiu, M. Kam, A. Javey and Z. Fan, *Nature*, 2020, **581**, 278.
2 G. Konstantatos, *Nat. Commun.*, 2018, **9**, 5266.
3 L. Su, T. Yan, X. Liu, F. Cao and X. Fang, *Adv. Funct. Mater.*, 2023, **33**, 2214533.
4 R. Xing, Z. Li, W. Zhao, W. D. Wang, R. Xie, R. Y. Chen, L. Wu and X. Fang, *Adv. Mater.*, 2024, **36**, 2310248.
5 W. Wang, M. Du, M. Zhang, J. Miao, Y. Fang and F. Zhang, *Adv. Opt. Mater.*, 2018, **6**, 1800249.
6 Z. Zhao, C. Xu, Y. Ma, K. Yang, M. Liu, X. Zhu, Z. Zhou, L. Shen, G. Yuan and F. Zhang, *Adv. Funct. Mater.*, 2022, **32**, 2203606.
7 M. Liu, Q. Yao, S. Li, Y. Qin, S. Y. Jeong, Y. Ma, L. Shen, X. Ma, K. Yang, G. Yuan, H. Y. Woo and F. Zhang, *Adv. Opt. Mater.*, 2024, **12**, 2303216.
8 A. Grillo, Z. Peng, A. Pelella, A. D. Bartolomeo and C. Casiraghi, *ACS Nano*, 2023, **17**, 1533.
9 A. Pelella, A. Grillo, E. Facella, G. Luongo, M. B. Askari and A. D. Bartolomeo, *ACS Appl. Mater. Interfaces*, 2021, **13**, 47895.
10 T. Lei, H. Tu, W. Lv, H. Ma, J. Wang, R. Hu, Q. Wang, L. Zhang, B. Fang, Z. Liu, W. Shi and Z. Zeng, *ACS Appl. Mater. Interfaces*, 2021, **13**, 50213.
11 O. Lopez-Sanchez, D. Lembke, M. Kayci, A. Radenović and A. Kis, *Nat. Nanotechnol.*, 2013, **8**, 497.
12 W. Deng, Y. Chen, C. You, B. Liu, Y. Yang, G. Shen, S. Li, L. Sun, Y. Zhang and H. Yan, *Adv. Electron. Mater.*, 2018, **4**, 1800069.
13 S. Gao, Z. Wang, H. Wang, F. Meng, P. Wang, S. Chen, Y. Zeng, J. Zhao, H. Hu, R. Cao, Z. Xu, Z. Guo and H. Zhang, *Adv. Mater. Interfaces*, 2020, **8**, 2001730.
14 P. Chang, S. Liu, Y. Lan, Y. Tsai, X. You, C. Li, K. Huang, A. Chou, C. Wu, J. Wang and C. Wu, *Sci. Rep.*, 2017, **7**, 46281.
15 D. De Fazio, I. Goykhman, D. Yoon, M. Bruna, A. Eiden, S. Milana, U. Sassi, M. Barbone, D. Dumcenco, K. Marinov, A. Kis and A. C. Ferrari, *ACS Nano*, 2016, **10**, 8252.
16 X. Feng, Z. He, W. Zhu, M. Zhao, Z. Liu, S. Yang, S. Tang, Q. Guo, Z. Jin, D. Chen, G. Ding and G. Wang, *J. Mater. Chem. C*, 2021, **9**, 609.

17 Y. Chien, T. L. Shen, W. Wu, C. Li, H. Chin, C. Chang, T. Lin, S. H. Chang, J. Shen and Y. Chen, *Mater. Today Nano*, 2022, **18**, 100173.
18 K. P. Bera, G. Haider, Y. Huang, P. K. Roy, C. R. P. Inbaraj, Y. Liao, H. Lin, C. Lu, C. Shen, W. Shih, W. Shih, Y. Chen, K. P. Bera, G. Haider, Y. Huang, P. K. Roy, C. R. P. Inbaraj, Y. Liao, H. Lin, C. Lu, C. Shen, W. Shih, W. Shih and Y. Chen, *ACS Nano*, 2019, **13**, 12540.
19 M. Massicotte, P. Schmidt, F. Vialla, K. G. Schädler, A. Reserbat-Plantey, K. Watanabe, T. Taniguchi, K. Tielrooij and F. H. L. Koppens, *Nat. Nanotechnol.*, 2015, **11**, 42.
20 Y. Chen, S. Chiu, D. Tsai, C. Liu, H. Ting, Y. Yao, H. Son, G. Haider, M. Kalbáč, C. Ting, Y. Chen, M. Hofmann and Y. Hsieh, *npj 2D Mater. Appl.*, 2022, **6**, 54.
21 S. R. K. C. Indukuri, C. Frydendahl, J. Bar-David, N. Mazurski and U. Levy, *ACS Appl. Nano Mater.*, 2020, **3**, 10226.
22 J. Li, J. Han, H. Li, X. Fan and K. Huang, *Mater. Sci. Semicond. Process.*, 2020, **107**, 104804.
23 W. Gao, S. Zhang, F. Zhang, P. Wen, L. Zhang, Y. Sun, H. Chen, Z. Zheng, M. Yang, D. Luo, N. Huo and J. Li, *Adv. Electron. Mater.*, 2020, **7**, 2000964.
24 L. Britnellf, R. M. Ribeiro, A. Eckmann, R. Jalil, B. D. Belle, A. Mishchenko, Y.-J. Kim, R. V. Gorbachev, T. Georgiou, S. V. Morozov, A. N. Grigorenko, A. K. Geim, C. Casiraghi, A. H. Castro Neto and K. S. Novoselov, *Science*, 2013, **340**, 1311.
25 C. Lan, C. Li, S. Wang, T. He, Z. Zhou, D. Wei, H. Guo, H. Yang and Y. Liu, *J. Mater. Chem. C*, 2017, **5**, 1494.
26 D. Krishnamoorthy and A. Prakasam, *J. Cluster Sci.*, 2020, **32**, 621.
27 R. Xiao, C. Lan, Y. Li, C. Zeng, T. He, S. Wang, C. Li, Y. Yin and Y. Liu, *Adv. Mater. Interfaces*, 2019, **6**, 1901304.
28 U. Sundararaju, M. A. S. M. Haniff, P. J. Ker and P. S. Menon, *Mater.*, 2021, **14**, 1672.
29 J. Y. Lin, F. C. Hsu, Y. C. Chao, J. W. Wu, Z. L. Yang, B. C. Huang, Y. P. Chiu and Y. F. Chen, *Small*, 2024, **21**, 2410990.
30 J. Lin, F. Hsu, C. Chang and Y. Chen, *J. Mater. Chem. C*, 2021, **9**, 5190.
31 C. Chang, H. Huang, H. Tsai, S. Lin, P. Liu, W. Chen, F. Hsu, W. Nie, Y. Chen and L. Wang, *Adv. Sci.*, 2021, **8**, 2002718.
32 L. Malard, M. Pimenta, G. Dresselhaus and Dresselhaus, *Phys. Rep.*, 2009, **473**, 51.
33 A. C. Ferrari and D. M. Basko, *Nat. Nanotechnol.*, 2013, **8**, 235.
34 Y. Cao, Z. Wang, Q. Bian, Z. Cheng, Z. Shao, Z. Zhang, H. Sun, X. Zhang, S. Li, H. Gedeon, L. Liu, X. Wang, H. Yuan and M. Pan, *Appl. Phys. Lett.*, 2019, **114**(13).
35 X. Zhang, X. Qiao, W. Shi, J. Wu, D. Jiang and P. Tan, *Chem. Soc. Rev.*, 2015, **44**, 2757.
36 K. Zhou, F. Withers, Y. Cao, S. Hu, G. Yu and C. Casiraghi, *ACS Nano*, 2014, **8**, 9914.
37 U. Bhanu, M. R. Islam, L. Tetard and S. I. Khondaker, *Sci. Rep.*, 2014, **4**, 5575.
38 I. Paradisanos, K. M. McCreary, D. Adinehloo, L. Mouchliadis, J. T. Robinson, H. Chuang, A. T. Hanbicki, V. Perebeinos, B. T. Jonker, E. Stratakis and G. Kioseoglou, *Appl. Phys. Lett.*, 2020, **116**, 203102.
39 J. Sitek, I. Pasternak, K. Czerniak-Łosiewicz, M. Świniarski, P. P. Michałowski, C. McAleese, X. Wang, B. R. Conran, K. Wilczyński, M. Macha, A. Radenović, M. Zdrojek and W. Strupiński, *2D Mater.*, 2022, **9**, 025030.
40 S. Kim, J. Kwak, J. H. Kim, J. Lee, Y. Jo, S. Kim, H. Cheong, Z. Lee and S. Kwon, *2D Mater.*, 2016, **4**, 011007.
41 Y. Chien, G. Lu, S. Li, Y. Chen, Y. Tsao, Y. Chao, J. Shen and Y. Chen, *Adv. Opt. Mater.*, 2024, **12**, 2302055.
42 W. Ortiz, C. Malca, D. Barrionuevo, A. Aldalbahi, E. Pacheco, N. Oli and P. Feng, *Vacuum*, 2022, **201**, 111092.
43 R. D. Jansen-van Vuuren, A. Armin, A. K. Pandey, P. L. Burn and P. Meredith, *Adv. Mater.*, 2016, **28**, 4766.
44 L. Dou, Y. M. Yang, J. You, Z. Hong, W.-H. Chang, G. Li and Y. Yang, *Nat. Commun.*, 2014, **5**, 5404.
45 C. Bao, Z. Chen, Y. Fang, H. Wei, Y. Deng, X. Xiao, L. Li and J. Huang, *Adv. Mater.*, 2017, **29**, 1703209.
46 Z. Huang, J. E. Carey, M. Liu, X. Gao, E. Mazur and J. C. Campbell, *Appl. Phys. Lett.*, 2006, **89**, 033506.
47 S. Xiong, L. Li, F. Qin, L. Mao, B. Luo, Y. Jiang, Z. Li, J. Huang and Y. Zhou, *ACS Appl. Mater. Interfaces*, 2017, **9**, 9176.
48 C. H. Ji, K. T. Kim and S. Y. Oh, *RSC Adv.*, 2018, **8**, 8302.
49 X. Gong, M. Tong, Y. Xia, W. Cai, J. S. Moon, Y. Cao, G. Yu, C.-L. Shieh, B. Nilsson and A. J. Heeger, *Science*, 2009, **325**, 1665.
50 B. H. Kim, H. Yoon, S. H. Kwon, D. W. Kim and Y. J. Yoon, *Vacuum*, 2021, **184**, 109950.
51 P. M. Pataniya and C. K. Sumesh, *ACS Appl. Nano Mater.*, 2020, **3**, 6935–6944.
52 C. W. Jang and S. Choi, *J. Alloys Compd.*, 2022, **901**, 163685.
53 J. Quereda, S. Kuriakose, C. Munuera, F. J. Mompean, A. M. Al-Enizi, A. Nafady, E. Diez, R. Frisenda and A. Castellanos-Gomez, *npj Flex. Electron.*, 2022, **6**, 23.
54 C. Labanti, J. Wu, J. Shin, S. Limbu, S. Yun, F. Fang, S. Y. Park, C. J. Heo, Y. Lim, T. Choi, H. J. Kim, H. Hong, B. Choi, K. B. Park, J. R. Durrant and J. Seon Kim, *Nat. Commun.*, 2022, **13**, 3745.
55 S. Li, Y. Zhang, W. Yang, H. Liu and X. Fang, *Adv. Mater.*, 2020, **32**, 1905443.
56 W. Song, J. Chen, Z. Li and X. Fang, *Adv. Mater.*, 2021, **33**, 2101059.
57 Y. Chen, L. Su, M. Jiang and X. Fang, *J. Mater. Sci. Technol.*, 2022, **105**, 259.
58 T. Yan, S. Cai, Z. Hu, Z. Li and X. Fang, *J. Phys. Chem. Lett.*, 2021, **12**, 9912.
59 Y. Ning, Z. Zhang, F. Teng and X. Fang, *Small*, 2018, **14**, 1703754.
60 J. Mao, Y. Yu, L. Wang, X. Zhang, Y. Wang, Z. Shao and J. Jie, *Adv. Sci.*, 2016, **3**, 1600018.
61 M. Alamri, M. Gong, B. Cook, R. Goul and J. Z. Wu, *ACS Appl. Mater. Interfaces*, 2019, **11**, 33390.
62 C. Zhou, S. Zhang, Z. Lv, Z. Ma, C. Yu, Z. Feng and M. Chan, *npj 2D Mater. Appl.*, 2020, **4**, 46.